Neutral and Charged 1-Butyl-3-methylimidazolium Triflate Clusters: Equilibrium Concentration in the Vapor Phase and Thermal Properties of Nanometric Droplets[†]

P. Ballone, C. Pinilla, J. Kohanoff, and M. G. Del Pópolo*

Queen's University Belfast, Atomistic Simulation Centre, Belfast BT7 1NN, UK

Received: November 12, 2006; In Final Form: January 4, 2007

Ground state energy, structure, and harmonic vibrational modes of 1-butyl-3-methylimidazolium triflate ([bmim]-[Tf]) clusters have been computed using an all-atom empirical potential model. Neutral and charged species have been considered up to a size (30 [bmim][Tf] pairs) well into the nanometric range. Free energy computations and thermodynamic modeling have been used to predict the equilibrium composition of the vapor phase as a function of temperature and density. The results point to a nonnegligible concentration of very small charged species at pressures ($P \sim 0.01$ Pa) and temperatures ($T \geq 600$ K) at the boundary of the stability range of [bmim][Tf]. Thermal properties of nanometric neutral droplets have been investigated in the $0 \leq T \leq 700$ K range. A near-continuous transition between a liquidlike phase at high T and a solidlike phase at low T takes place at $T \sim 190$ K in close correspondence with the bulk glass point $T_g \sim 200$ K. Solidification is accompanied by a transition in the dielectric properties of the droplet, giving rise to a small permanent dipole embedded into the solid cluster. The simulation results highlight the molecular precursors of several macroscopic properties and phenomena and point to the close competition of Coulomb and dispersion forces as their common origin.

I. Introduction

Favorable environmental properties and a remarkable potential for applications have made imidazolium ionic compounds key players in the emerging field of green chemistry.[1] A common feature shared by most of these systems is their relatively low melting temperature, underlying their extensive usage as solvents and reflected in the *room-temperature ionic liquid* (RTIL) label collectively attributed to them.

Recently, the range of potential applications of RTILs has been greatly extended by the experimental demonstration of RTIL distillation,[2] opening the way to innovative extraction and purification processes.[3] In addition to its impact on applications, the successful distillation of RTILs provide a new and powerful reason of interest for their vapor phase, directly responsible for the mass transfer during distillation. Of immediate concern, of course, are the macroscopic thermodynamic properties of the vapor under a wide range of pressure and temperature conditions. A deeper understanding and a fine control of all parameters, however, requires a more microscopic approach based on the identification of all the species present in the vapor, as well as a precise determination of their relative stability and reaction kinetics.

As a first step toward this goal, we report here the results of a comprehensive computational investigation of small neutral and charged 1-butyl-3-methylimidazolium triflate ([bmim][Tf], see Figure 1) clusters. Ground state energies and geometries for an extended set of cluster composition and sizes have been determined using computer simulation based on an empirical force field. The equilibrium concentration of all species in the vapor phase has been computed using chemical equilibrium relations. The choice of [bmim][Tf] among the many compounds
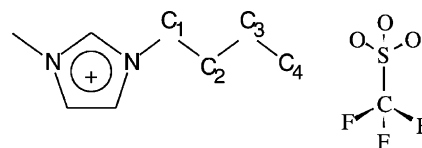

Figure 1. Schematic view of the [bmim][Tf] structure.

whose distillation was reported in ref 2 is motivated by the prototypical role of [bmim] $^+$ among RTIL cations and by the extended temperature range of stability for the [bmim][Tf] salt.

The results reveal an intriguing and complex picture involving competing interactions and diverse structural motifs and prompted us to extend our study to larger clusters (up to 30 ion pairs) and to a broader range of properties and conditions. Although absent in the equilibrium vapor at any realistic pressure and temperature, neutral and charged nanometric RTIL droplets are readily created by electrospraying[4] as well as by a variety of low-energy bombardment techniques, including electron, ion, and fast atom bombardment.[5] Once created, these ionic systems are natural candidates to be analyzed by modern beam[6,7] and electrostatic trap techniques as well as by a variety of spectroscopic techniques using high-intensity (laser or synchrotron) light sources.

Reasons of interest in nanometric and subnanometric RTIL aggregates include subjects of both fundamental and applied relevance and include the identification of stability peaks corresponding to specific growth patterns; the investigation of the interplay of Coulomb and dispersion interactions in finite RTIL systems; the size-dependence of the several phase transitions observed in macroscopic samples, ranging from the liquid to liquid-crystal transition;[8] and the paraelectric-to-ferroelectric transitions observed in some RTILs.[9] Additional reasons of interest concern the harmonic and dissipative dynamics in finite Coulomb systems and the thermodynamics and kinetics of fission and evaporation from multiply charged clusters. Exotic potential applications involving RTIL clusters

---

[bmim][Tf] Clusters

J. Phys. Chem. B, Vol. 111, No. 18, 2007 **4939**

include ionic propulsion,[10] plasma-phase power generation, nanostructured materials, and nanometric ferroelectric systems and devices.[11]

II. Computational Method

The structural optimization of clusters, as well as the equilibrium simulations, is based on the all-atom empirical force field defined in ref 12 and parametrized in ref 13 (see also ref 14). To prevent the evaporation of ions during the long simulation cycles described below, each cluster, either neutral or charged, is enclosed into a weak confining potential.[15]

The accuracy and reliability of the potentials of ref 13 has already been demonstrated in a growing number of applications reported in the literature. As a further test, we verified that the potential is able to reproduce the experimental lattice parameters of the [bmim][Tf] crystal.[16,17] The validity of a rigid ion model is supported by the low value ($\epsilon_\infty = 2.05$, see ref 18) of the high-frequency dielectric constant of [bmim][Tf], suggesting that electron polarization effects are modest.

Molecular dynamics (MD) and Monte Carlo (MC) have been used as the primary tools to explore and sample the configuration space of [bmim][Tf] clusters. Simulations have been performed using both a standard package[19] and homemade MD and MC programs.

Harmonic vibrational properties around the local energy minima identified by our optimization procedure have been determined by diagonalizing the dynamical matrix computed via a finite difference approximation to the second derivative of the energy with respect to the atomic positions.

Benchmark density functional (DF) computations for the smallest species have been performed using the CPMD[20] code. Both implementations include explicitly valence states only, replacing the valence core interaction by suitable pseudopotentials.[21] The exchange and correlation energy has been approximated using a standard generalized gradient approximation (GGA-PBE).[22]

The determination of low-energy structures has been by far the most time-consuming part of our investigation. The global optimization problem underlying the search of ground state geometries is known to be intrinsically difficult in all cases. However, it becomes particularly challenging for molecular species such as [bmim][Tf], since the fairly high number of atoms and the constraints imposed by the bond topology multiply the number of local minima, enhance the barriers among them, and greatly extend relaxation rates. As a result, we do not claim that the lowest energy structures described below are, indeed, the global minima of their respective potential energy surfaces (PES). Nevertheless, a long sequence of simulations using a combination of different methods and the fair reproducibility of the optimization results make us confident that the structures we found are close in energy to the true ground state and include the relevant properties and geometric motifs of the ideal lowest energy structure. In other words, we think that the structures we find are representative of the low-energy portion of the PES, even though they are likely to differ from the global energy minimum in their detailed structure.

A first optimization attempt consisted of fairly long (20 ns) MD simulated annealing (SA) cycles performed on a sequence of neutral and charged clusters. A constant annealing rate was applied, starting from $T = 640$ K and going down to $T \sim 20$ K. The resulting energies and structures displayed clear anomalies as a function of size, pointing to insufficient optimization. To overcome this major limitation, we resorted to the basin-hopping

technique[23] and to a MC strategy tuned on the specific properties of the [bmim][Tf] system.

Our basin-hopping implementation consists of a sequence of large random displacements of all the atoms, followed by an efficient and robust local optimization of the energy. This strategy produced a few of the lowest energy structures discussed below. Nevertheless, most of the optimization has been performed with a specialized MC−SA implementation, since this strategy allowed us to collect thermodynamic data while optimizing structures and because the efficiency of the method turned out to be sufficient for our purposes. Our MC implementation includes, in addition to the usual single atom moves, a set of whole-ion translations and rotations, significantly enhancing the mean square displacement per unit of computation time. More importantly, it includes the discrete sampling of rotational isomers for the butyl tail, which are nearly degenerate and represent an important source of complexity. In this way, our ad hoc procedure is able to move efficiently among low-energy basins without sampling directly the barriers separating them. The validity of this strategy is demonstrated by the fairly high acceptance ratio for these moves, by the high mean square displacement of the ions, and by the low energies systematically obtained by our SA cycles. Typical MC−SA cycles consisted of a sequence of $\sim$30 constant-temperature runs, uniformly distributed in the $0 < T \leq 640$ K range. Considering all types of MC moves, the displacement of each atom was attempted $\sim$2 × 10⁶ times during each run. Monte Carlo estimates of equilibrium properties have been obtained with runs of comparable length with an almost equal number of equilibration and production steps.

Molecular dynamics with ad hoc constraints[24] has been used to investigate a variety of structural and thermodynamic properties. We used it, in particular, to compute the free energy profile along a reaction coordinate, following the prescriptions of ref 25.

III. Simulation Results

We report in this section our results for the energy, structure, and vibrational and thermal properties of [bmim][Tf] nanoclusters. In what follows, the size of individual clusters is specified by an ordered pair of integers in parentheses (n^+, n^-), giving the number of cations and anions, respectively.

A. Low-Energy Structures. Structural optimization has been carried out for a series of neutral clusters of size up to (30, 30), and for a short sequence of cationic clusters $(n + 1, n)$ and anionic clusters $(n, n + 1)$ with $n = 0, ..., 10$. The first cluster property we analyze is the cohesive energy, defined here as the energy required to split the cluster into its constituent ions. This quantity, therefore, includes a fairly large contribution corresponding to the energy required to separate neutral pairs into anions and cations, and this choice partly influences the discussion of cohesive properties contained in this section. A different but equivalent picture is obtained by referring the computation of cohesion to the energy of the neutral pairs. The two descriptions, however, are easily interchanged into each other using the data on the cohesive energy of the (1, 1) cluster reported below.

The cohesive energy per ion for the structures of lowest energy found for each of these aggregates is shown in Figure 2 as a function of $1/N^{1/3}$, where $N = n^+ + n^-$ is the total number of ions in the cluster. At variance from what is observed in elemental clusters, the size dependence of the energy is very regular, without apparent stability peaks pointing to a sequence of *magic numbers* and to an underlying structural growth motif.
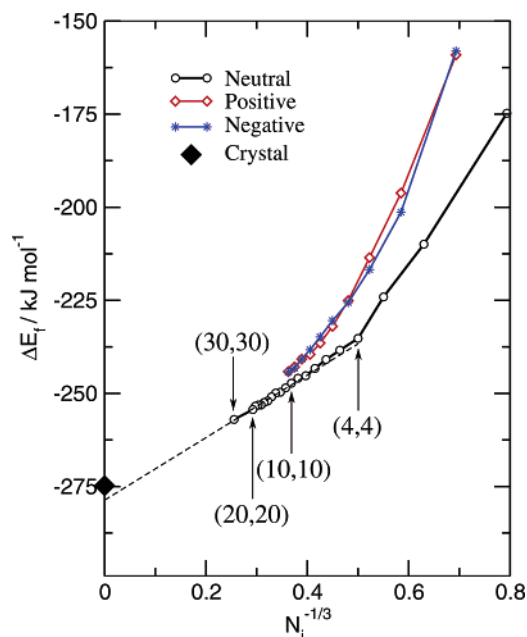
4940 *J. Phys. Chem. B, Vol. 111, No. 18, 2007*

Ballone et al.

Figure 2. Cohesive energy per ion of neutral and singly charged [bmim][Tf] clusters as a function of $1/N^{1/3}$, where $N = n^+ + n^-$ is the total number of ions in the (n^+, n^-) cluster. The solid lines are a guide to the eye. The dashed line is a linear interpolation for the energy of neutral clusters larger than (12, 12). The energy of the crystal (black diamond) has been computed using the same potential and computational framework used for the clusters.

In fact, excluding the smallest clusters with up to ∼8 ions, the energy of the neutral species displays a remarkably linear dependence on $1/N^{1/3}$, which represents the leading term of the so-called *leptodermic* expansion for the energy of finite systems. The extrapolation of the neutral cluster data to the thermodynamic limit $N \to \infty$ (or equivalently, $N^{-1/3} \to 0$) provides an estimate for the bulk cohesive energy very close (see Figure 2) to the energy computed for the experimental crystal structure relaxed with the same force field, enhancing our confidence in the reliability of the optimization strategy. The results for charged clusters are expected to tend to the same energy in the thermodynamic limit, although the data reported in Figure 2 are not sufficient to unambiguously confirm this property.

The slope of the linear E versus $1/N^{1/3}$ dependence estimated for neutral aggregates is directly related to the surface energy of [bmim][Tf] at $T = 0$ K, and a simple computation gives $e_s = 84.8$ mJ/m². This value is, of course, an average surface energy, accounting for the many (defective) surface orientations delimiting the clusters. The available experimental data for similar RTILs range from $e_s = 57.6$ mJ/m² for [bmim][BF$_4$] to $e_s = 69.2$ mJ/m² for [bmim][PF$_6$].[26] It appears, therefore, that our computational value for [bmim][Tf] is on the high-energy side of measured surface energies for [bmim]-based RTILs. However, it is important to note that the experimental values have been measured in the liquid phase at $T = 336$ K, whereas our result refers to $T = 0$ K. Even though the experimental plots of e_s versus temperature show that e_s is remarkably constant in the liquid phase, an increase in the surface energy can be expected in going from the liquid to the solid phase. This argument suggests that the computational result provides a meaningful prediction of e_s for [bmim][Tf] at low T. This tentative conclusion is particularly remarkable and encouraging, taking into account the limited size range and the limited number of structural optimizations required to obtain the e_s estimate.
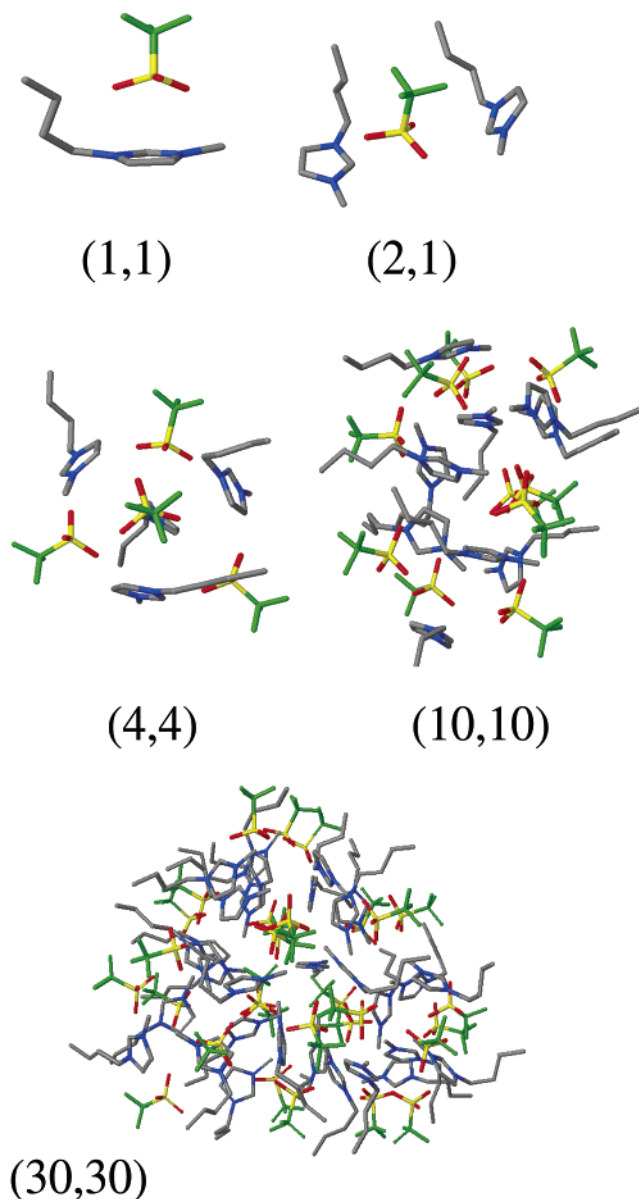

Figure 3. Lowest energy structure for selected neutral and charged clusters found by the optimization procedure described in the text.

The absence of stability peaks corresponding to closed shells of ions might, in principle, be an artifact of an incomplete structural optimization. We think, however, that this is a genuine property of these moderately complex ionic−organic systems. First of all, the flexibility of the basic ionic building block (especially in the [bmim]$^+$ case) provides the system with a dense and nearly continuous distribution of local energy minima, allowing a smooth evolution along the size progression. Moreover, although the complexity of the PES is likely to prevent us from finding the true global minimum, we observe that our optimization procedure reliably and consistently produces structures whose energy differs by 0.02 kJ/atom at most, equivalent to a temperature of only a few K. For this reason, although we expect that our incomplete optimization affects the precise atomic positions and symmetry of the resulting structure, we nevertheless think that the optimal energies provide a tight upper bound for the ideal ground state energy.

The lowest energy geometry of selected clusters is shown in Figure 3. As already mentioned, no strict regularity or symmetry is observed, although a few general features are apparent in all

[bmim][Tf] Clusters

J. Phys. Chem. B, Vol. 111, No. 18, 2007 **4941**

TABLE 1: Inertia Moments of Neutral Clusters along the Principal Axes of Inertia[a]

size	I_1	I_2	I_3
(1, 1)	2360	1734	1027
(2, 2)	7275	6652	4005
(3, 3)	16 961	12 779	10 880
(4, 4)	23 550	21 126	18 234
(5, 5)	33 485	30 293	25 616
(6, 6)	42 882	41 522	34 639
(7, 7)	64 087	61 762	40 850
(8, 8)	80 856	73 164	49 178
(9, 9)	96 992	78 134	69 081
(10, 10)	123 361	104 694	75 143
(11, 11)	139 984	137 838	81 374
(12, 12)	151 445	127 033	110 486
(13, 13)	161 083	144 535	138 053
(14, 14)	174 089	161 765	155 073
(15, 15)	202 088	193 662	159 038
(16, 16)	260 033	245 487	160 513
(17, 17)	279 317	256 981	176 323
(18, 18)	275 478	269 443	218 321
(19, 19)	312 448	259 451	254 863
(20, 20)	353 936	332 611	239 148
(30, 30)	640 532	597 950	531 792

[a] Mass is measured in units of the H mass, and distances, in Å.

the optimal structures. All clusters are fairly rounded, or more precisely, they display a rotation ellipsoid geometry, with prolate and oblate shapes nearly equally represented (See Table 1).

In all cases, anions and cations do not appear to be associated into closely bonded pairs. In this respect, [bmim][Tf] clusters behave as genuine ionic systems starting from the smallest possible sizes. However, there are also apparent violations of the strict charge alternation that dominates the structure of traditional inorganic ionic systems, confirming that the strength of Coulomb interactions in RTIL is relatively weak, and other energy contributions play a significant role (see Section 3.6 below).

Excluding again the smallest clusters, the sequence of optimized structures displays a nearly continuous evolution with increasing size and prevents the identification of a clear growth sequence.

The analysis of snapshots shows that the surface of neutral clusters up to (30, 30) is populated both by [bmim]$^+$ and [Tf]$^-$ions (see Figure 4a), even though it appears to be somewhat enriched in the [Tf]$^-$ ions. Moreover, the butyl tail and especially the CF$_3$ termination of [Tf]$^-$ tend to stick out of the surface, whereas the imidazolium rings tend to be hidden immediately below the surface. These results are in qualitative agreement with the experimental measurements of ref 26. Moreover, they are qualitatively similar to those reported in ref 27 on the surface structure of the different but related [bmim][Tf$_2$N] liquid. In addition, the orientation of different structural units appears to follow clear trends: both the butyl tail and the sulfur-carbon axis of [Tf] tend to align in the radial direction (see Figure 4b), whereas the imidazole ring displays a slight preference for a tangential orientation at the cluster surface. This orientation of individual ions is likely to be determined by the rounded shape and small size of clusters, and the qualitative picture described above is expected to become quickly less relevant with increasing cluster size, eventually merging into the description of the extended liquid or solid surface of RTIL, whose general properties have been discussed in detail in ref 28.

The butyl tail can be found in a variety of rotational isomers. Particularly noteworthy is the cis−trans isomerization around the C$_1$−C$_2$ bond (see Figure 1) closely related to the polymorphism of [bmim][Cl] and [bmim][Br] crystals.[29,30] In low-energy clusters, both the cis and the trans forms are present, however,
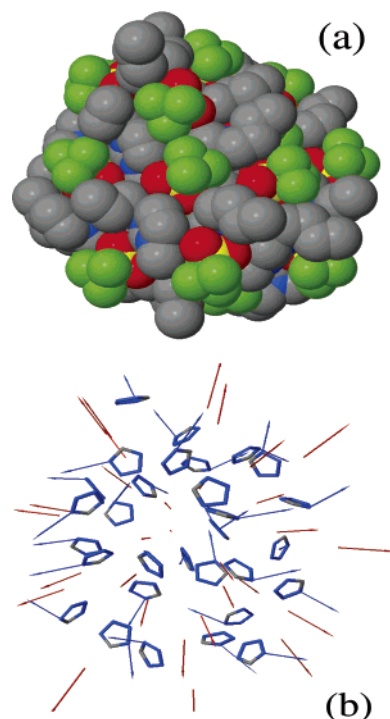

Figure 4. (a) A different picture of the (30, 30) ground state structure. Black particles, carbon; blue, nitrogen; red, oxygen; green, fluorine; yellow, sulfur. Hydrogen atoms are not shown. (b) Schematic view of the same (30, 30) cluster highlighting the orientation of the major structural elements. The blue arrows join the C4−C1 positions of [bmim]$^+$, and represent the alkyl tail. The red arrows are directed along the C−S axis of [Tf]$^-$.

with a clear predominance of the cis form, typically accounting for 80% of the [bmim]$^+$ ions.

As expected, the ground state electrostatic dipole of neutral [bmim][Tf] clusters is generally low and does not display any clear trend as a function of size. Our computations predict a dipole moment of 14.8, 9.7, 9.7, and 24.0 Debye for the (1, 1), (10, 10), (20, 20) and (30, 30) clusters, respectively.

The optimal structures found for charged ions do not differ in any remarkable way from that of neutral clusters, and also in this case, it is difficult to identify a clear growth motif. The $T = 0$ ionization potentials, easily computed from the data of Figure 2 (see also Table 2 below), do not display any remarkable behavior. Only the neutral (4, 4) cluster might enjoy a stability advantage with respect to its ionized forms larger than in the case of other clusters. Once again, the multicenter and many-body character of the interaction among the basic ionic bonds is responsible for the continuous evolution of structures and energies as a function of charge as well as size.

B. Thermal Properties and Ion Concentrations in the Vapor. As stated in the introduction, the experimental demonstration of distillation reported in ref 2 provided the major motivation for the present study. The equilibrium concentration of neutral and charged clusters in the vapor results from the combined effect of all possible fusion/fission elementary reactions:

$$(1, 0) + (0, 1) \rightleftharpoons (1, 1)$$

$$(1, 1) + (1, 0) \rightleftharpoons (2, 1)$$

$$\ldots \qquad\qquad (1)$$
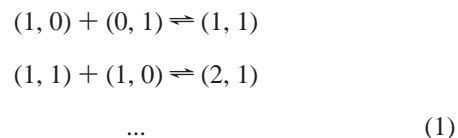
collectively represented by the simple A + B $\rightleftharpoons$ C equation. According to elementary kinetic theory, at equilibrium, the

TABLE 2: Free Energy Differences for a Series of Elementary Reactions A + B ⇌ C Computed at $T = 400$ K and at $T = 0$ K[a]

reaction	ΔF ($T = 400$ K) (kJ/mol)	ΔF ($T = 0$ K) (kJ/mol)
$(0, 1) + (1, 0) \rightleftharpoons (1, 1)$	-321 ± 5	-349.5
$(1, 2) + (1, 0) \rightleftharpoons (2, 2)$	-353 ± 5	-365.6
$(2, 3) + (1, 0) \rightleftharpoons (3, 3)$	-335 ± 13	-337.9
$(3, 4) + (1, 0) \rightleftharpoons (4, 4)$	-362 ± 8	-364.7
$(4, 5) + (1, 0) \rightleftharpoons (5, 5)$	-366 ± 11	-353.7
$(5, 6) + (1, 0) \rightleftharpoons (6, 6)$	-368 ± 8	-351.9
$(2, 1) + (0, 1) \rightleftharpoons (2, 2)$	-348 ± 9	-362.5
$(2, 3) + (0, 1) \rightleftharpoons (3, 3)$	-363 ± 9	-363.6
$(4, 3) + (0, 1) \rightleftharpoons (4, 4)$	-380 ± 11	-387.9
$(5, 4) + (0, 1) \rightleftharpoons (5, 5)$	-376 ± 21	-358.2
$(6, 5) + (0, 1) \rightleftharpoons (6, 6)$	-374 ± 21	-339.0
$(1, 1) + (1, 0) \rightleftharpoons (2, 1)$	-113 ± 3	-127.7
$(2, 2) + (1, 0) \rightleftharpoons (3, 2)$	-129 ± 8	-141.2
$(3, 3) + (1, 0) \rightleftharpoons (4, 3)$	-158 ± 10	-149.4
$(4, 4) + (1, 0) \rightleftharpoons (5, 4)$	-157 ± 15	-143.8
$(5, 5) + (1, 0) \rightleftharpoons (6, 5)$	-163 ± 9	-168.0
$(1, 1) + (0, 1) \rightleftharpoons (1, 2)$	-112 ± 2	-123.6
$(2, 2) + (0, 1) \rightleftharpoons (2, 3)$	-170 ± 9	-166.8
$(3, 3) + (0, 1) \rightleftharpoons (3, 4)$	-180 ± 6	-172.5
$(4, 4) + (0, 1) \rightleftharpoons (4, 5)$	-198 ± 13	-148.2
$(5, 5) + (0, 1) \rightleftharpoons (5, 6)$	-187 ± 11	-151.0

[a] At $T = 0$, the free energy differences are equal to the corresponding total energy differences, ΔE.

concentrations [A], [B], [C] of species A, B, and C, respectively, satisfy the relation

$$\frac{[C]}{[A][B]} = k_{eq} = \exp[-\beta \Delta F(T)] \quad (2)$$

where $\Delta F = F(C) - F(A) - F(B)$ is the free energy difference driving the reaction, $\beta = 1/K_B T$, and K_B is the Boltzmann constant. The free energy difference ΔF consists of an ideal part, ΔF_{id}, and a configurational part, ΔF_{conf}. The former is computed by a simple rigid body model for the system kinetic energy, and the latter is computed by atomistic simulation (see Appendix I).
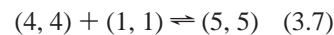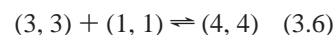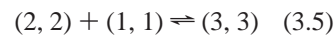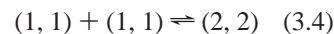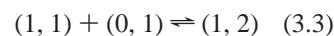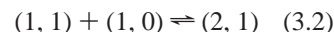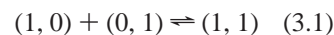
The configurational free energy differences computed at $T = 400$ K are collected in Table 2, where they are compared to their $T = 0$ counterpart (i.e., the corresponding ground state energy differences). Statistical error bars have been estimated by dividing each simulation into six parts and computing the standard deviation of the corresponding subaverages. As is apparent from Table 2, the estimated error bars are fairly large, but the results display a remarkable degree of self-consistency, highlighted by the following observation: a given pair of initial and final species can be joined by a variety of hypothetical reaction paths involving different elementary reactions and intermediate species. The final free energy difference has to be the same irrespective of the reaction path from reactants to products. We verified that this is, indeed, the case for the reactions of Table 2, at least within the estimated error bars.

Two observations are immediately apparent. First of all, removing one ion from a neutral cluster, thus creating two oppositely charged species, requires a large amount of energy. Therefore, and as expected, ionized species will appear at nonnegligible concentrations only at high temperatures or very low densities, when large entropic contributions favor fragmentation. On the other hand, removing a neutral pair costs much less energy. As a result, the equilibrium of neutral clusters is displaced toward small species. Moreover, a close inspection of Table 2 shows that the reaction free energy ΔF at $T = 400$ K is well approximated by the corresponding $T = 0$ K value,

given by the ground state energy difference ΔE. More precisely, we find that $|\Delta E|$ is systematically larger than $|\Delta F|$ for reactions involving very small species only, but $|\Delta E| < |\Delta F|$ for larger aggregates. The crossover between these opposite trends takes place for clusters of about six ions.

The similarity of $|\Delta E(T = 0)|$ and $|\Delta F(T)|$ over a wide temperature range is a nontrivial observation resulting from the close compensation of large but nearly equivalent temperature variations of both potential energy and entropy for all the species involved in each reaction. However, chemical reactions change the subdivision of ions within different aggregates, and they are expected to affect significantly interionic interactions. The mild variations of ΔF with increasing T, therefore, suggests that thermal properties of [bmim][Tf] clusters are dominated by intramolecular contributions, with intermolecular terms playing only a relatively minor role.

These two observations guide our choice of the theoretical framework used to compute the concentrations. First of all, we limit the number of species considered in our computations to the smallest species expected to appear in sizable concentration. The final set of independent reactions we consider is as follows:

$$(1, 0) + (0, 1) \rightleftharpoons (1, 1) \quad (3.1)$$

$$(1, 1) + (1, 0) \rightleftharpoons (2, 1) \quad (3.2)$$

$$(1, 1) + (0, 1) \rightleftharpoons (1, 2) \quad (3.3)$$

$$(1, 1) + (1, 1) \rightleftharpoons (2, 2) \quad (3.4)$$

$$(2, 2) + (1, 1) \rightleftharpoons (3, 3) \quad (3.5)$$

$$(3, 3) + (1, 1) \rightleftharpoons (4, 4) \quad (3.6)$$

$$(4, 4) + (1, 1) \rightleftharpoons (5, 5) \quad (3.7)$$

$$(5, 5) + (1, 1) \rightleftharpoons (6, 6) \quad (3.8) \quad (3)$$

The corresponding kinetic equations, 3.1–3.8, are supplemented by a relation setting the total density and a second equation imposing charge neutrality, providing a closed set of 10 relations among the ten unknown concentrations [(1, 0)], [(0, 1)], [(1, 1)], [(2, 1)], [(1, 2)], [(2, 2)], [(3, 3)], [(4, 4)], [(5, 5)], and [(6, 6)].

As a further simplification, we replace the temperature-dependent configurational free energy differences with $T = 0$ potential energy differences, since these are less affected by error bars and are already available at the end of the optimization stage without requiring further computations and further modeling. The resulting nonlinear equations for the cluster densities are solved using a standard computer algebra code.[31]

In what follows, the total density is treated as an independent variable, and we shall characterize the system as being in the *gas* phase (instead of the vapor phase), to emphasize the fact that the system is not in equilibrium with an underlying condensed phase, either liquid or solid.

The results for the density of all major species are collected in Figure 5 for two distinct values of the total system density, equal to $\rho_1 = 10^{-5}$ mol/m³ (panel a) and $\rho_2 = 10^{-7}$ mol/m³ (panel b). These two densities are lower than those estimated in the distillation experiment ($\sim 2 \times 10^{-2}$ mol/m³) of ref 2, but well within the range of equilibrium densities reported in ref 32 and measured at comparable temperatures. We observe that, as expected, larger species are favored at low temperature, stabilized by their enhanced cohesive energy. Particularly abundant is the (4, 4) cluster, apparently because of its cohesive energy advantage coupled to a relatively small size, thus
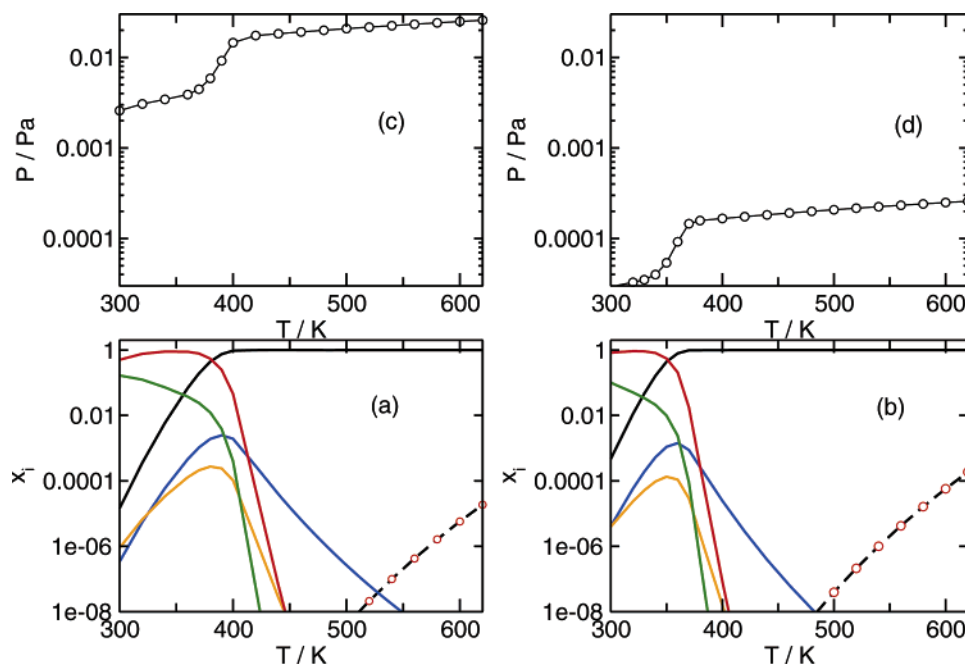
[bmim][Tf] Clusters

J. Phys. Chem. B, Vol. 111, No. 18, 2007 **4943**

Figure 5. Molar fraction of neutral and charged species in the gas phase at two different densities: (a) $\rho_1 = 10^{-5}$ mol/m³; (b) $\rho_2 = 10^{-7}$ mol/m³. Full curves: neutral species. Black line, (1, 1); blue, (2, 2); orange, (3, 3); red, (4, 4), green, (5, 5). Charged species: black dashed line, (1, 0); red circles, (0, 1). Total pressure as function of T. (c) $\rho_1 = 10^{-5}$ mol/m³ ; (d) $\rho_2 = 10^{-7}$ mol/m³.

optimizing both potential energy and entropy contributions. At high temperature ($T \geq 500$ K), the neutral monomer (1, 1) accounts for the near totality of the system mass, but sizable concentrations of small charged species appear at $T \geq 600$ K. The nonmonotonic temperature variations of the density for all other intermediate species results from the close competition of potential energy, favoring larger aggregates and prevailing at low T, and entropy, favoring small species and prevailing at high T. The results on concentrations provide an estimate of the gas pressure as a function of T, assuming again an ideal gas relation between the density of each species and its partial pressure. The results are collected in Figure 5 (panel c for ρ_1, and panel d for ρ_2). At both densities, the most noticeable feature is the sharp rise of pressure at $T \sim 400$ K, resulting from the thermal break-up of the (4,4) cluster. This feature, therefore, reflects the shifting chemical equilibrium with increasing T and cannot be interpreted as pointing to an incipient phase transition in the dilute gas.

C. Harmonic Dynamics. The optimized structures described in Sec. 2.1 provide the starting point for the computation of harmonic vibrational frequencies and eigenmodes.

The density of states (DOS) for selected sizes ((1, 1), (10, 10), (30, 30)) is shown in Figure 6, which contains also the vibrational DOS for the orthorhombic crystal phase of [bmim]-[Tf].[33] This last has been determined by the same computational scheme used for clusters, considering a $2 \times 2 \times 2$ supercell replica[34] of the experimental unit cell given in ref 16. The dipolar character of the modes, closely related to their infrared activity, is quantified by computing the size of the dipole, p_α, induced by the atomic displacements of mode α. The dipole-weighted DOS, computed by assigning a weight $|p_\alpha|^2$ to each mode, is represented in Figure 6 by the shaded area superimposed to the DOS of the (30, 30) cluster. As expected, the dipolar character tends to increase with increasing frequency of the modes. A residual dipolar character, however, is observed down to the lowest frequencies, with a small but not negligible peak at a frequency as low as $\omega \sim 60$ cm^{-1}.

The size dependence of the DOS is apparently minor, suggesting that most of the features apparent in Figure 6 are,

in fact, related to intramolecular vibrations, whereas intermolecular interactions are responsible only for slight frequency shifts distributed along the entire spectrum and possibly larger but still difficult-to-identify changes at very low frequency ($\omega \leq 100$ cm^{-1}). This picture is confirmed by a detailed analysis of the displacement vectors, showing that for all sizes and for most modes, only a handful of atoms belonging to the same ion account for most of the mode displacement. Only at very low frequency, modes delocalized over the entire cluster are found, and these delocalized modes are expected to be the most affected by the intermolecular interactions.

To gain further insight into the low-energy portion of the spectrum and to identify features related to the intermolecular interactions, we introduce a reduced harmonic Hamiltonian having as independent variables the coordinates and momenta of the center of mass (CM) of individual [bmim]$^+$ and [Tf]$^-$ ions. Starting from a local energy minimum, defining a corresponding configuration for the CM's positions, the second derivative of the energy with respect to the CM's coordinates is computed by displacing the CM of the corresponding [bmim]$^+$ or [Tf]$^-$ ions and then carefully relaxing all atomic coordinates under the constraint of fixed CM positions. This projection from the original to the reduced harmonic Hamiltonian corresponds to considering the ions as effective particles interacting with each other via effective many-body potentials implicitly defined by our constrained minimization. The reduced Hamiltonian can also be seen as describing the adiabatic dynamics of individual atoms adapting quickly to the slow motion of the whole ions.

The DOS of the reduced harmonic Hamiltonian is reported in Figure 7 for the (2, 2) and (10, 10) clusters. The eigenfrequencies of the reduced harmonic Hamiltonian cover the relatively narrow frequency range $0 \leq \omega \leq 90$ cm^{-1}. The size dependence of the reduced DOS is now a major effect, suggesting that our projection techniques provides an effective view of intermolecular interactions and can be used to explore the evolution of vibrational properties with increasing system size.

The drastic reduction in vibrational frequency in going from the full to the reduced Hamiltonian justifies a posteriori the
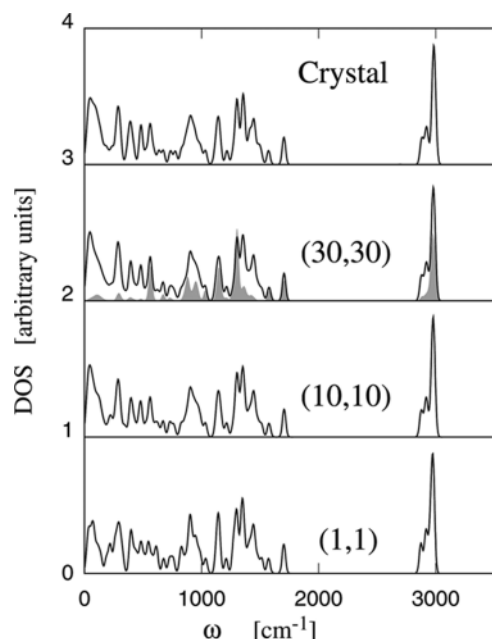
Figure 6. Vibrational density of states (DOS) for selected clusters and for the [bmim][Tf] crystal. The shaded area within the (30, 30) curve represents the DOS weighted by the square length of the dipole induced by the mode displacement.
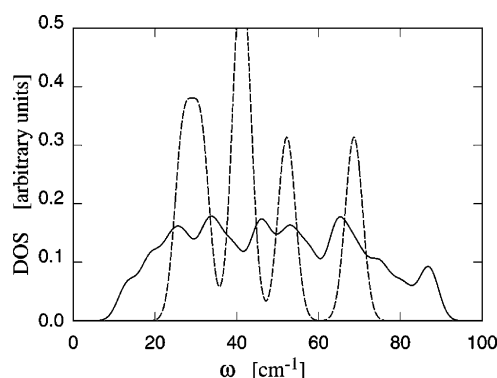

Figure 7. Density of states for the reduced harmonic Hamiltonian describing interion displacements (see text). Dashed line, (2, 2) cluster; solid line, (10, 10) cluster.

adiabatic approximation underlying the projection scheme. It is partly due to the fairly large mass of the ions, but also to the relatively soft effective ion−ion interactions, which are shown in Figure 14 for the case of the [bmim][bmim] and [bmim][Tf] pairs (see also Appendix II). The displacement of the ions described by the eigenvectors of the reduced Hamiltonian reproduces the patterns familiar from more traditional ionic systems (such as NaCl clusters, see ref 6). The highest frequency mode at $\omega \sim 90$ cm^{-1}, in particular, is associated with the largest induced dipole moment, and it is the most likely candidate to evolve into the bulk plasmon mode with increasing cluster size.

Unfortunately, the computational cost of the repeated constrained optimization required by the projection scheme outlined above grows rapidly with increasing cluster size. A simplified scheme in which the displacement of the CMs is performed without the successive constrained optimization of the atomic positions provides a qualitatively similar picture, but it overestimates the corresponding frequencies by ~30% for the high-frequency modes and by more than a factor of 2 in the low-frequency range.

D. Thermal Properties of Nanometric Droplets. We complement our discussion of the relative stability for the
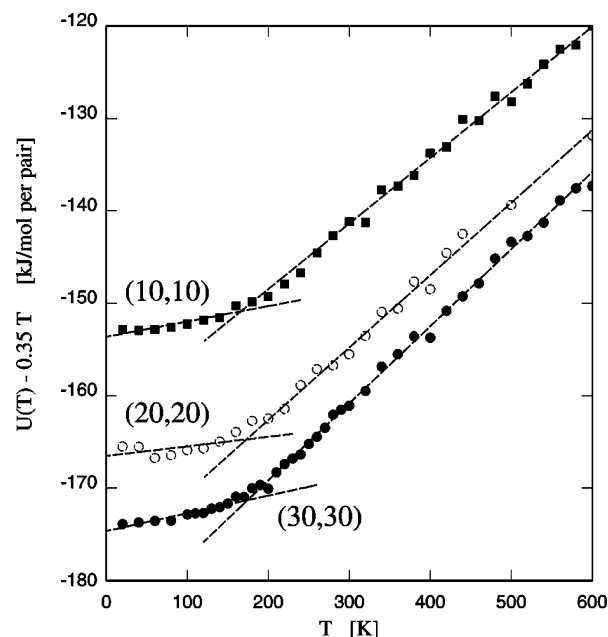

Figure 8. Average potential energy per neutral ion pair U as a function of T for the (10, 10), (20, 20), and (30, 30) clusters. The same linear term $U_{lin} = 0.35T$ has been subtracted from each curve. The dashed lines are a linear interpolation for the low- and high-temperature portions of $U(T)$.
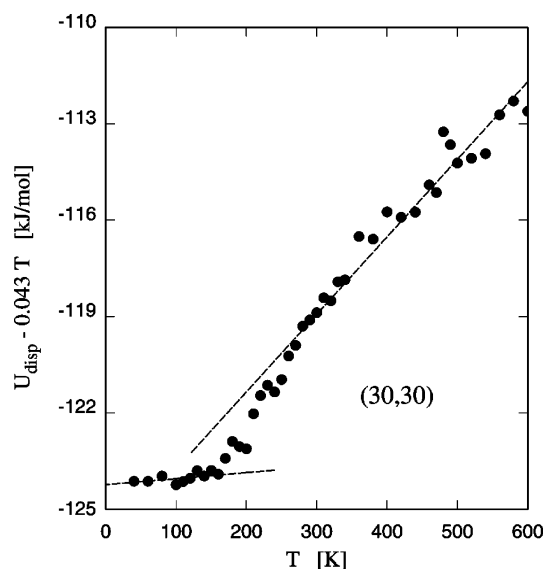

Figure 9. Average dispersion energy $(-C_6/r^6)$ per neutral [bmim][Tf] pair as a function of T for the (30, 30) cluster.

smallest [bmim][Tf] clusters with a broad exploration of thermal properties of the larger species (from (10, 10) to (30, 30)), seen as prototypical nanometric RTIL droplets.

The potential energy of selected cluster sizes is reported in Figure 8 as a function of temperature in the range $0 \leq T \leq 640$, corresponding to the stability range of [bmim][Tf], which decomposes at $T \geq 700$ K.[35] To highlight the relevant information contained in these data, we subtracted the same linear term ($U_{lin} = 0.35T$, U is in kJ/mol, T is in K) from each curve. In all cases, the average potential energy displays two distinct linear ranges at low and at high temperature. No (near-) discontinuity or marked anomaly is observed around $T = 286$ K, corresponding to the melting temperature of bulk [bmim][Tf].[35]

The continuous but fairly sharp transition between the two linear regimes is highly reminiscent of a glass transition as it appears in computational investigations of amorphous materi-
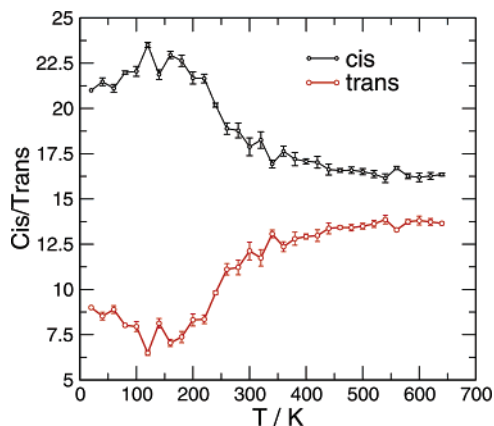
[bmim][Tf] Clusters

J. Phys. Chem. B, Vol. 111, No. 18, 2007 **4945**

Figure 10. Average number of cis and trans isomers in the (30, 30) cluster as a function of temperature.
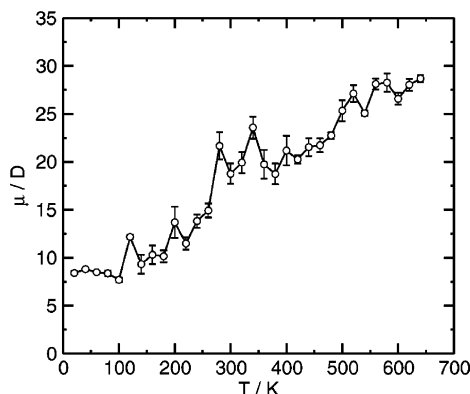

Figure 11. Average length of the electrostatic dipole moment for the (30, 30) cluster as a function of temperature. The solidlike structures (below $T \sim 200$ K) obtained in these simulations do not correspond to the lowest energy geometry.
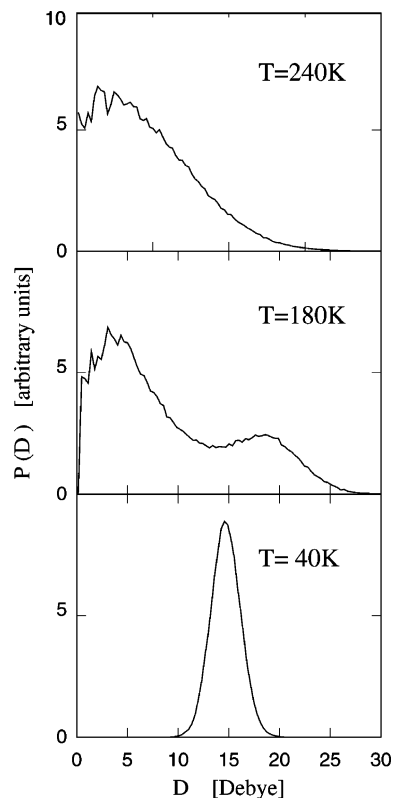

Figure 12. Probability distribution for the length D of the electrostatic dipole moment of a (20, 20) cluster at three different temperatures. The solidlike structures (below $T \sim 200$ K) obtained in these simulations do not correspond to the lowest energy geometry.

als.[36] Moreover, the glass transition temperature estimated from the crossing of the low- and high-temperature linear interpolations progresses from $T_g = 180$ K for the (10, 10) cluster to $T_g = 185$ K for (20, 20) and, finally, to $T_g = 188$ K for (30, 30). Since the glass transition temperature of bulk [bmim][Tf] is expected to be close to $T_g = 200$ K,[35] it is tempting to conclude that the continuous transition seen in our simulations is, indeed, the precursor of the bulk glass transition, whose T_g temperature can be estimated by extrapolating the finite cluster data. This conclusion, although very appealing, is likely to underestimate the complexity of these systems and of their phase transitions, and we suspect that the close correspondence between the computed and measured glass transition might result from accidental compensation of errors due, for instance, to the fairly simple interatomic potential, the short time scale of the simulation, and the small size of the simulated systems.

A different, although not completely incompatible, interpretation is suggested by a more detailed analysis of the thermal behavior of these systems. The temperature dependence of individual contributions to the potential energy (i.e., the Coulomb energy, the dispersion interactions, the short-range repulsion, or the intramolecular energy terms) all show anomalies around $T = 200$ K. The general character of these individual transformations, however, is closer to a weakly discontinuous transition (see Figure 9), taking place at slightly different temperatures for the different energy contributions. This last feature, together with the fact that the individual energy jumps are fairly small, gives rise to the nearly continuous change of slope in the U-versus-T curve at $T \sim 190$ K, which, however,

conceals a transition whose character is weakly discontinuous. This interpretation is consistent with the structural results discussed in Section 3.1, pointing to apparently disordered low-energy structures incorporating, however, marked regularities.

Analysis of the mobility of atoms estimated by both MC and MD shows that the change in slope of the $U(T)$ curves corresponds to a drastic drop of diffusion. We shall call this transformation *solidification*, without a clear distinction between a glass transition and a weak and defective crystallization.

Computer simulation often provides access to structural properties difficult to measure in experiments. An example is the computation of the proportion of cis and trans isomers of [bmim]$^+$ around the C_1-C_2 bond of Figure 1 in the (30, 30) cluster as a function of temperature (see Figure 10). Starting from a nearly equiconcentration of the two isomers at high T, the cis form becomes increasingly dominant with decreasing temperature. Only small variations of the relative concentration of cis and trans isomers are observed below $T \sim 190$, corresponding to the solidification point.

A subject of increasing interest is the presence of ferroelectric transition(s) in crystals of room temperature RTILs.[9] Computer simulations of clusters provide an interesting opportunity to investigate how a permanent dipole could (or could not) arise in a finite system free of strict boundary constraints, whose structure, moreover, is either glassy or at least highly defective. To characterize the dielectric signature of [bmim][Tf] clusters, we computed the average length $D = |D|$ of their electrostatic dipole moment as a function of temperature. The data for the (30, 30) cluster are plotted in Figure 11, showing that the dipole moment decreases significantly and monotonically with decreasing temperature, which is consistent with the well-known fact that a sizable dipole is associated with a large electrostatic energy.
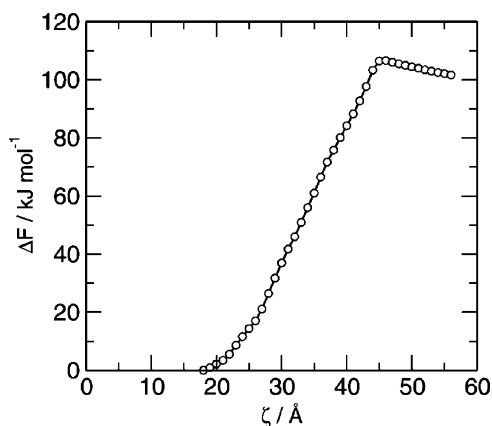
Figure 13. Free-energy profile along the reaction coordinate leading from a doubly charged (20, 18) cluster to two separated ((18, 17) and (2,1)) clusters. The reaction coordinate corresponds to the distance between two tagged cations. The peak at $\zeta = 45$ Å corresponds to the breaking point.
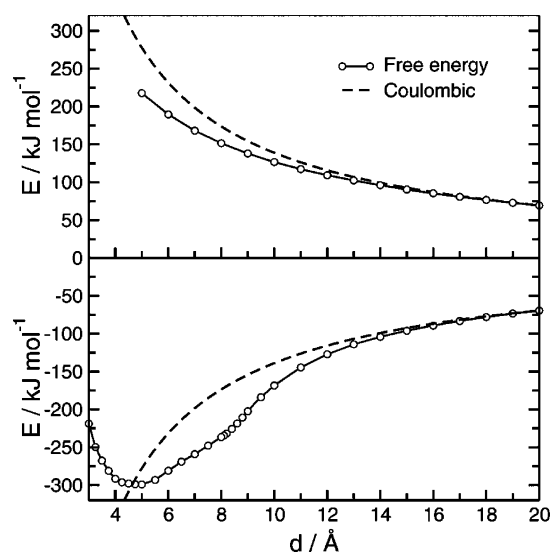

Figure 14. Potential of mean force between [bmin]$^+$ and [Tf]$^-$ ions computed at $t = 400$ K. Upper panel: [bmin]$^+$−[bmin]$^+$. Lower panel: [bmin]$^+$−[Tf]$^-$. The dashed curves in both panels represent the corresponding Coulomb potentials for point charges.

More revealing is the analysis of the probability distribution $P(D)$ for the instantaneous length D of the cluster dipole moment, shown in Figure 12 for the (20, 20) cluster at three different temperatures. The probability, $P(D)$, is defined in such a way that the average length, $\langle D \rangle$, of the dipole moment is given by

$$\langle D \rangle = \frac{\int_0^\infty DP(D)D^2 \, dD}{\int_0^\infty P(D)D^2 \, dD}$$

At the highest temperature ($T = 240$ K), $P(D)$ is approximatively Gaussian, as expected for the fluctuating dipole of a liquidlike system. At the lowest temperature ($T = 40$ K), the cluster is solidlike and has acquired a relatively small permanent dipole moment, which fluctuates slightly because of the thermal movement of the atoms. Interestingly, we found an intermediate regime ($T = 180$ K) where the distribution function $P(D)$ is apparently bimodal, pointing to the coexistence of a solidlike domain carrying an embedded permanent dipole and a liquidlike component giving rise to a Gaussian background in $P(D)$. Once

again, the transition between the two regimes takes place around the solidification point identified in the $U(T)$ curves.

E. Metastability of Doubly Charged Clusters. As a last stage of our exploration of [bmim][Tf] cluster properties, we comment on the (meta-) stability of doubly charged RTIL droplets. Whereas only very small and singly ionized species appear in the equilibrium vapor at any sizable concentration, multiply charged clusters and droplets could arise from more energetic phenomena, such as ion or electron bombardment,[5] or could result from fragmentation and evaporation following electrospraying.[37] Our simulations suggest that once formed, and provided they are not too small, multiply charged clusters might display very long average lifetimes. Starting from a (20, 20) cluster well equilibrated at $T = 400$ K, we removed two [Tf]$^-$ anions, and we let the system evolve by MD in the microcanonical ensemble. We verified that the double charge made the system thermodynamically unstable, since the average energy of the doubly charged cluster greatly exceeds the sum of two singly charged clusters of half the original size. In other words, splitting the (20, 18) cluster into two (10, 9) clusters decreases significantly the system energy. Moreover, ideal entropy favors the two separate clusters over the single aggregate configuration, further destabilizing the doubly charged moiety. Despite these unfavorable conditions, the doubly charged (20, 18) cluster survived as long as we could run our simulation, covering a time span of 50 ns. A more quantitative assessment on the (meta) stability of the (20, 18) cluster is obtained by exploring a reaction coordinate, ζ, whose growth eventually forces the doubly charged cluster to split into two singly charged entities. This coordinate, ζ, has been chosen to be the separation between two tagged cations. Progressively extending ζ during a sequence of constrained MD simulations at first deforms the (20, 18) cluster into a stretched ellipsoidal geometry, and eventually it causes its breakup into the (18, 17) and (2, 1) fragments. Being unconstrained by the simulation algorithm, the choice of this highly asymmetric breaking channel is apparently determined by the cluster kinetics. The free energy profile as a function of ζ is shown in Figure 13. The breaking of the original (20, 18) cluster occurs at $\zeta = 45$ Å, corresponding to the peak in the free energy profile. At much larger distances the computed curve has to merge into the repulsive Coulomb energy, e^2/ζ, of two ions of equal charge $|e|$ at distance ζ. Apparent transformations of the structure and bonding pattern take place immediately before fragmentation. These phenomena and other important features of the fragmentation mechanism and kinetics are still in the process of being quantitatively analyzed.

F. Insight into the Bonding of [bmim][Tf]. The sequence of optimal energies and geometries discussed in Sec. 3.1 provides an excellent opportunity to gain insight into the relative role of different energy contributions in the bonding and structural organization of [bmim][Tf] condensed systems.

Starting from the isolated [bmim]$^+$ and [Tf]$^-$ ions, the formation of the neutral (1, 1) pair is driven by a large Coulomb energy gain of 343 kJ/mol and a much smaller dispersion energy advantage of 13.5 kJ/mol. Repulsive energy and intramolecular terms increase slightly, but together do not change the energy balance by more that a few kilojoules per mole. The total energy gain of 349.5 kJ/mol in the neutral pair formation (see Table 2) is close to the DF−CPMD estimate of 335.7 kJ/mol.

Beyond this initial step, the relative role of Coulomb and dispersion forces changes drastically, especially along the (n, n) sequence of neutral clusters. For instance, joining two

[bmim][Tf] Clusters

J. Phys. Chem. B, Vol. 111, No. 18, 2007 **4947**

neutral pairs giving rise to the (2, 2) cluster improves the Coulomb energy by 95 kJ/mol, but the dispersion energy term now contributes a substantial 41 kJ/mol.

The addition of a neutral pair to a neutral (n, n) cluster larger than (4, 4) gives rise to a dispersion energy gain that is ~75% of the Coulomb energy gain, highlighting the comparable role of Coulomb and dispersion forces in RTIL compounds. This is at variance with the case of traditional inorganic ionic salts, in which Coulomb interactions are by far the dominant binding force. Moreover, analysis of the Lennard−Jones coefficients in the potential and numerical evidence from energy computations show that dispersion interactions in [bmim][Tf] clusters concern mainly the butyl tails, with a significant but smaller role for the imidazole ring. This near equivalence of Coulomb and short-range attraction underlies a variety of structural and thermodynamic properties of RTIL and [bmim][Tf] in particular, including their tendency to form liquid mesophases made of charge-alternating nanodomains[38,39] and the peculiar crystal structure of [bmim][Cl] and [bmim][Br] displaying ordered columnar arrangements of [bmim]$^+$ ions optimizing the close range interaction of their butyl tails. Similar geometric arrangements are found along the entire alkylimidazolium family (See the review by Y.-F. Hu and C.-M. Xu in ref 18) and probably arising from the same energy considerations.

The relative role of Coulomb and dispersion interactions is reflected also in the energy ordering of different cluster isomers. Starting from the smallest species (including [bmim]$^+$), we observe that the relative stability of different isomers is often decided by the dispersion energy term, which is far more structure-sensitive and -selective than the longer-range Coulomb energy.

Unfortunately, density functional computations are of limited value in quantifying the fine details of the potential energy surface and in verifying/tuning the model potentials. First of all, the dispersion interactions, playing an important role in these systems, are neglected in the most popular local and semilocal DF approximations, including PBE. Moreover, the energy difference among the isomers of interest is so small ($\Delta E \leq 1$ kJ/mol) to be below the confidence limit of methods based on the total energy of the full valence electron system.

Further insight into the complementary and sometimes competing role of Coulomb and dispersion forces is obtained by two simple computer experiments. Setting all atomic charges to 0 reduces the cluster cohesion by roughly a factor of 2. More importantly, these artificially neutralized clusters rapidly give rise to the segregation of [bmim] and [Tf] into different cluster subdomains, underlying the role of Coulomb forces in keeping [bmim]$^+$ and [Tf]$^-$ into close contact and the tendency of dispersion forces to precipitate the fairly highly cohesive [bmim] component.

A direct test of the role of dispersion interactions is obtained by redefining the short range nonbonded interaction as

$$V_{SR}(r) = \begin{cases} 4\epsilon\left[(\sigma/r)^{12} - (\sigma/r)^6 + \dfrac{1}{4}\right] & \text{if } r \leq 2^{1/6}\sigma \\ 0 & \text{if } r > 2^{1/6}\sigma \end{cases}$$

The $V_{SR}(r)$ potential, consisting of only the repulsive part of the original Lennard−Jones potential, is continuous and has continuous first derivative. This modification of the short range interaction, removing the attractive part of dispersion interactions enhanced the mixing of [bmim]$^+$ and [Tf]$^-$, but also causes a telling morphology change in clusters that now assume the needlelike shape characteristic of systems bound by purely dipolar forces. Analysis of snapshots shows that, indeed, the system is made of closely bound [bmim]$^+$ and [Tf]$^-$pairs.

Weak hydrogen bonds linking H in the imidazole ring to electron-rich atoms on another ion have been extensively discussed in the literature as important energy and structural elements.[40] Although the tendency of imidazole-hydrogens to approach negatively charged atoms is apparent in all simulated structures, these links never appear in our computations as well-defined bonds, especially if we require the distance and directional selectivity of genuine hydrogen bonds. Moreover, we remark that the large softening of the highest frequency modes characteristic of hydrogen bond formation is absent in the vibrational spectra of Figure 6. However, taking into account the weak strength of these interactions, these results might say more about the approximate nature of the potentials we used in our simulations than about the reality of bonding in [bmim]-[Tf] clusters.

IV. Summary and Concluding Remarks

A broad exploration of structural and dynamical properties of [bmim][Tf] aggregates has been carried out using computer simulation. The results provide a first comprehensive picture of RTIL clusters, extending in size well into the nanometric range and covering most of the temperature range over which [bmim][Tf] is stable.

The first stage of our study has been devoted to the identification of low-energy configurations. Our investigation has confirmed the extreme difficulty of finding the global minimum of the potential energy surface for these systems, far exceeding the challenge posed by inorganic clusters of comparable or even larger size.[41] This is apparently related to the constraints introduced by intramolecular bonds, greatly enhancing the barriers separating different potential energy basins. Advanced techniques and specific SA implementations tuned on the structural properties of [bmim][Tf] have been used to partly overcome this difficulty. Nevertheless, a sequence of very long simulations has been required to provide a consistent set of results.

The major outcome of the optimization stage for [bmim][Tf] is a sequence of low-energy structures for neutral and ionized clusters with up to 30 ion pairs displaying a fairly smooth variation of the ground state energy with cluster size and charge. Only the (4, 4) cluster might enjoy a sizable enhanced stability with respect to neutral and ionized species of comparable size. The soft interaction among flexible ionic units and the collective character of cohesion in these clusters is the most likely responsible for the observed smooth variation of energy and structures with increasing size.

Almost without exceptions, the ground state structures consist of mixtures of different rotational isomers for the [bmim]$^+$ tail, confirming that the associated multitude of near degenerate configurations is an important source of entropy for these systems.

The concentration of small [bmim][Tf] species in the gas phase has been estimated by computing the free energy differences for all the relevant reactions. This allows us to determine the concentration of neutral and charged species as a function of the gas density and temperature. The results displayed in Figure 5 show that, as expected, the vapor is made mainly by neutral [bmim][Tf] single pairs. Nevertheless, the concentration of tetramers is nonnegligible, and ionized species appear at ~10^{-4} molar fraction for temperatures $T \sim 600$ K, still within the chemical stability range for [bmim][Tf]. Even though a 10^{-4} free ions molar fraction might seem (and is)

small, it is, nevertheless, larger than in most condensed matter systems at comparable temperatures and low density.

The harmonic vibrational spectrum is dominated by intramolecular modes. This is hardly surprising, since the degrees of freedom describing the relative position and motion of the constituent [bmim]$^+$ and [Tf]$^-$ions is a small subset of all atomic coordinates. Nevertheless, we devised a method able to project the total mode populations onto the relevant degrees of freedom, identified as the centers of mass of the individual ions. The simple mapping described in Section 3.3 provides a coherent picture of intermolecular modes and highlight a close relation with typical bulk spectral properties, such as the plasma oscillations.

The constant temperature simulation of nanometric [bmim]-[Tf] droplets allowed us to investigate the transition from the high-temperature, liquidlike state to a solidlike state at low T. At first sight, the transition appears to be a continuous one, similar to the glass transition of extended systems. A closer look, however, suggests that the transition is weakly first order, perhaps analogous to an incomplete crystallization. Moreover, we investigated in detail how a permanent dipole moment arises during the cluster solidification. Simulation results reveal a temperature range in which liquidlike and solidlike domains coexist, leading to a bimodal probability distribution $P(D)$ for the length D of the dipole moment. Coexistence is, in principle, possible only in finite (and possibly small) systems, and it is expected to fade away quickly with increasing cluster size.

As a further step, we investigated by MD the stability/metastability character of multiply charged clusters. The results of these simulations, together with the free energy data already discussed, could allow a fully computational prediction of evaporation/condensation rates for [bmim][Tf] droplets, with possible implications on a variety of subjects, such as electrospraying, Coulomb explosion, aerosol formation, and stability.

As a final point, we analyze the role of different energy contributions in determining the observed properties of [bmim]-[Tf] clusters. As expected, all the simulation results point to the complementary and sometimes competing role of Coulomb and dispersion forces that in RTILs seem to have comparable strength. This result motivates a strong note of caution concerning the usage of standard density functional approximations for the computational prediction of RTIL cluster properties.[42] Most of the standard recipes lack dispersion energy terms, and the cluster geometries predicted by these methods might differ significantly from the real ones.

The results obtained in our investigation provide interesting insight into a variety of subjects related to RTIL systems, both extended and finite. We shall consider in detail a few of these connections in the future, looking for quantitative comparison with experiments. Preliminary computations for clusters of a different RTIL, that is, [dmim]-Cl have already been performed, using both the potential of ref 13 and the potential of ref 43. The results, displaying an intriguing combination of similarities and differences with the [bmim][Tf] case, will be reported elsewhere.

V. Appendix I: Computation of Reaction Free Energies

The prototypical A + B ⇌ C reaction considered in Sec. 3.2 reaches an equilibrium state determined by the free energy difference $\Delta F(T) = F_C(T) - F_A(T) - F_B(T)$, as discussed above. Each individual free energy contribution is given by

$$F(T) = -K_B T \log Q(T) \tag{4}$$

where $Q(T)$ is the system partition function, defined by an integral over the coordinates and momenta of all the atoms in the system. According to classical statistical mechanics, the partition function $Q(T)$ can be factorized into an ideal part, Q_{id}, arising from the integration over the momenta, and a configurational part, Q_{conf}, defined by the integration over coordinates.

The ideal part Q_{id} is computed by representing the [bmim][Tf] species appearing in the chemical reactions of Section 3.2 as rigid bodies, whose shape is summarized by the three independent momenta of inertia I_x, I_y, I_z. The particle kinetic energy accounts for translations of the center of mass and for rigid body rotations. This allows us to write[44]

$$Q_{id}(T) = \Delta^t(T)\Delta^R(T) \tag{5}$$
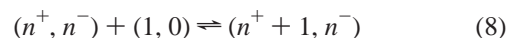
where

$$\Delta^t(T) = \left(\frac{2\pi M K_B T}{h^2}\right)^{3/2} \tag{6}$$

$$\Delta^R(T) = \pi^{1/2}\left(\frac{8\pi^2 K_B T}{h^2}\right)^{3/2}(I_x I_y I_z)^{1/2} \tag{7}$$

The mass M in eq 6 is the total mass of the aggregate. The momenta of inertia, in principle dependent on temperature, are approximated by the values computed for the ground state configurations (see Table 1). Although approximate, the inclusion of rotational contributions to the partition function is strictly required to obtain a meaningful and reliable estimate for the equilibrium concentrations.

The computation of the configurational functions is by far the most time-consuming part of the determination of equilibrium concentrations in the gas phase. The simple addition/removal character of the elementary reactions considered in Section 3.2 already suggests resorting to a variant of the Widom's insertion/deletion method[45] for a one-pass evaluation of the configurational part of the free energy difference, ΔF. Let us consider, for instance, the addition of a positive ion to the (n^+, n^-) cluster:

$$(n^+, n^-) + (1, 0) \rightleftharpoons (n^+ + 1, n^-) \tag{8}$$

In what follows, $\{U^{(l^+,l^-)}\}$ and $\{d\mathbf{r}^{(l^+,l^-)}\}$ represent the potential energy and the configuration space element for the (l^+, l^-) cluster. Then, one can write

$$\frac{Q^{(n^+,n^-)}Q^{(1,0)}}{Q^{(n^++1,n^-)}} = \exp[\beta\Delta F] =$$

$$\frac{d\mathbf{r}^{(n^+,n^-)}\exp[-\beta U^{(n^+,n^-)}]\,d\mathbf{r}^{(1,0)}\exp[-\beta U^{(1,0)}]}{d\mathbf{r}^{(n^++1,n^-)}\exp[-\beta U^{(n^++1,n^-)}]} \tag{9}$$

A simple rearrangement gives

[bmim][Tf] Clusters

J. Phys. Chem. B, Vol. 111, No. 18, 2007 **4949**

$$\exp[\beta\Delta F(T)] = \frac{\int \, d\mathbf{r}^{(n^++1,n^-)} \exp[-\beta U^{(n^++1,n^-)}] \exp[\beta\Delta U]}{d\mathbf{r}^{(n^++1,n^-)} \exp[-\beta U^{(n^++1,n^-)}]} \tag{10}$$

where

$$\Delta U = U^{(n^++1,n^-)} - U^{(n^++1,n^-)} - U^{(1,0)} \tag{11}$$

represents the interaction binding the additional ion to the original cluster.

Equation 10 is equivalent to

$$\exp[\beta\Delta F(T)/K_B T] = \langle \exp[\beta\Delta U]\rangle_{(n^++1,n^-)} \tag{12}$$

where the $\langle ...\rangle_{(n^++1,n^-)}$ bracket indicates thermal averaging over the distribution function for the $(n^+ + 1, n^-)$ cluster.

Therefore, the sought-for free energy difference can be evaluated by averaging the function $\exp[\beta\Delta U]$ during a MD or MC simulation for the larger $(n^+ + 1, n^-)$ cluster. Our scheme differs from the original Widom's method only because the particle added or removed is not a simple, structureless particle, but a complex ion with its own temperature-dependent partition function.

The implementation of these relations using MD has highlighted once again the positive and negative features of the Widom's method, shared by the closely related umbrella algorithm.[45] On one hand, the method provides a direct and computationally convenient estimation of free energy differences, requiring a single temperature simulation without thermodynamic integration to include the entropy contribution. On the other hand, because of the rapidly varying exponential integrand, the result is determined mainly by a few favorable configurations for which ΔU is not too negative. As a consequence, fluctuations tend to be large, increasing the final error bar.

The results provided by the Widom's method have been verified in a few cases using thermodynamics integration to evaluate entropy differences. The results agree with those provided by the Widom method within the estimated error bar.

VI. Appendix II: Ion−Ion Potentials of Mean Force

A simple representation of the interactions determining structural and dynamic properties of clusters can be obtained by the most drastic coarse-graining procedure, replacing [bmim]$^+$ and [Tf]$^-$ ions with spherical and structureless particles centered at the CM of the ions and interacting with effective pair potentials. The pairwise interactions are defined a priori by considering a pair of ions, constraining the distance of their CMs to a fixed value and averaging their potential energy with respect to all remaining degrees of freedom. The inter-ion potentials obtained in this way, however, display marked anomalies with spikes and cusps, since the constrained averaging gives rise to close contacts and to bistable configurations. These anomalies are easily and effectively removed by performing the required averaging at nonzero temperature. The simplest procedure, implemented in our computation, is based on the prescriptions of ref 25 and starts with the computation of the average force on the CMs as a function of their distance. By definition, the potential of mean force is the integral of this average force and provides a meaningful measure of the interaction between two complex units as a function of their distance.

The results for the [bmim][bmim] and [bmim][Tf] pairs obtained by averaging at $T = 400$ K are shown in Figure 14.

Both effective potentials lay below the bare Coulomb term, at least before the short-range repulsion sets in. The extra attraction is provided by dispersion forces but, even more, by electrostatic correlation, optimizing the mutual orientation of the two approaching ions. The most remarkable feature apparent in Figure 14 is the broad, attractive well displayed by the [bmim]-[Tf] potential. The low curvature at the minimum together with the fairly large mass of the ions corresponds well to the low-frequency ion−ion oscillations highlighted by the projection scheme described in Section 3.3. The effective ion−ion potential in larger clusters has certainly a many-body character, but the pair potential part defined here is expected to represent its major contribution.

Supporting Information Available: Vibrational frequencies (in cm^{-1}) for the (1, 0), (0, 1), (1, 1), and (2, 2) clusters are provided in a single ASCII file. This material is available free of charge via the Internet at http://pubs.acs.org.

References and Notes

(1) *Ionic liquids: Industrial applications for green chemistry*; Rogers, R. D., and Seddon, K. R., Eds.; American Chemical Society: Washington DC, 2002.

(2) Earle, M. J.; Esperanca, J. M. S. S; Gilea, M. A.; Canongia Lopes, J. N.; Rebelo, L. P. N.; Magee, J. W.; Seddon, K. R.; Widegren, J. A. *Nature* **2006**, *439*, 831−834. Rebelo, L. P. N.; Canongia Lopes, J. N.; Esperanca, J. M. S. S.; Filipe, E. *J. Phys. Chem. B* **2005**, *109*, 6040−6043.

(3) See also: Wasserscheid, P. *Nature* **2006**, *439*, 797.

(4) Fenn, J. B.; Mann, M.; Meng, C. K.; Wong, S. F.; Whitehouse, C. M. *Science* **1989**, *246*, 64−71.

(5) Abdul-Sada, A. K.; Elaiwi, A. E.; Greenway, A. M.; Seddon, K. R. *Eur. Mass Spectrosc.* **1997**, *3*, 245−247.

(6) Early molecular beam investigations of traditional ionic systems such as alkali and alkali-earth halides are reviewed in: Martin, T. P. *Phys. Rep.* **1983**, *95*, 167−199.

(7) Lozano, P. C. *J. Phys. D: Appl. Phys.* **2006**, *39*, 126−134.

(8) Binnemans, K. *Chem. Rev.* **2005**, *105*, 4148−4204.

(9) Pajak, Z.; Czarnecki, P.; Szafranska, B.; Maluszynska, H.; Fojud, H. *Phys. Rev. B: Condens. Matter Mater. Phys.* **2004**, *69*, 132102.

(10) Gamero-Castano, M.; Hruby, V. *J. Propul. Power* **2001**, *17*, 977−987.

(11) Gruverman, A.; Kholkin, A. *Rep. Prog. Phys.* **2006**, *69*, 2443−2474.

(12) Jorgensen, W. L.; Maxwell, D. S.; Tirado-Rives, J. *J. Am. Chem. Soc.* **1996**, *118*, 11225−11236.

(13) Canongia Lopes, J. N.; Deschamps, J.; Padua, A. A. H. *J. Phys. Chem. B* **2004**, *108*, 2038−2047. Canongia Lopes, J. N.; Padua, A. A. H. *J. Phys. Chem. B* **2004**, *108*, 16893−16898. See also (Additions and corrections): Canongia Lopes, J. N.; Deschamps, J.; Padua, A. A. H. *J. Phys. Chem. B* **2004**, *108*, 11250.

(14) It is important to note that the mixing rules for the Lennard−Jones coefficients adopted in ref 13 are $\sigma_{ij} = \sqrt{\sigma_{ii}\sigma_{jj}}$ and $\epsilon_{ij} = \sqrt{\epsilon_{ii}\epsilon_{jj}}$ and differ from the popular Berthelot rules. Canongia Lopes, J. N.; and Padua, A. A. H. private communication. This point is discussed and clarified in: Canongia Lopes, J. N.; Padua, A. A. H. *J. Phys. Chem. B* **2006**, *110*, 19586−19592.

(15) The confining potential identically vanishes within a sphere whose radius R is significantly larger than the expected cluster radius. For $r > R$, the potential is given by $V_{conf} = \alpha(r - R)^2$, with $\alpha = 0.1$ kJ/mol/Å^2.

(16) Choudhury, A. R.; Winterton, N.; Steiner, A.; Cooper, A. I.; Johnson, K. A. *J. Am. Chem. Soc.* **2005**, *127*, 16792−16793.

(17) The computed lattice parameters are $a = 10.318$, $b = 12.243$, $c = 21.877$, $\alpha = 90.47$, $\beta = 97.52$, and $\gamma = 90.114$ (lengths are in Å, and angles, in degrees) to be compared with the experimental values: $a = 10.222$, $b = 12.534$, $c = 22.541$, $\alpha = 90.0$, $\beta = 93.281$, and $\gamma = 90.0$).

(18) Arce, A.; Rodriguez, H.; Soto, A. *Fluid Phase Equilib.* **2006**, *242*, 164−168. A low dielectric constant $\epsilon_\infty \sim 2$ is a property shared by most RTIL; see: Hu, Y.-F.; Xu, C.-M. *Chem. Rev.* **2006**, in press.

(19) Smith, W.; Leslie, M.; Forester, T. R. *DL−POLY*, v2.14; Daresbury Laboratories: Daresbury, Warrington WA4 4AD, U.K., 2003.

(20) Computations have been performed using the CPMD 3.0 program, written by J. Hutter; Max-Planck-Institut für Festkörperforschung: Stuttgart, 1996.

(21) Troullier, N.; Martins, J. L. *Phys. Rev. B: Condens. Matter Mater. Phys.* **1991**, *43*, 1993−2006.

(22) Perdew, J. P.; Burke, K.; Ernzerhof, M. *Phys. Rev. Lett.* **1996**, *77*, 3865−3868.

(23) Wales, D. J.; Doye, J. P. K. *J. Phys. Chem. A* **1997**, *101*, 5111−5116.

(24) Ryckaert, J. P.; Ciccotti, G.; Berendsen, H. J. C. *J. Comput. Phys.* **1977**, *23*, 327−341.

(25) Mülders, T.; Krüger, P.; Swegat, W.; Schlitter, J. *J. Chem. Phys.* **1996**, *104*, 4869−4870.

(26) Law, G.; Watson, P. R. *Langmuir* **2001**, *17*, 6138−6141.

(27) Höfft, O.; Bahr, S.; Himmerlich, M.; Krischok, S.; Schaefer, J. A.; Kempter, V. *Langmuir* **2006**, *22*, 7120−7123.

(28) Lynden-Bell, R. M.; Del Pópolo, M. G. *Phys. Chem. Chem. Phys.* **2006**, *8*, 949−954.

(29) Holbrey, J. D.; Reichert, W. M.; Nieuwenhuyzen, M.; Johnston, S.; Seddon, K. R.; Rogers, R. D. *Chem. Comm.* **2003**, 1636−1637.

(30) Hayashi, S.; Ozawa, R.; Hamaguchi, H. *Chem. Lett.* **2003**, *32*, 498−499. Saha, S.; Hayashi, S.; Kobayashi, A.; Hamaguchi, H. *Chem. Lett.* **2003**, *32*, 740−741. A short review on [bmim][Cl] and [bmim][Br] polymorphism is contained in: Hamaguchi, H.-O.; Ozawa, R. *Adv. Chem. Phys.* **2005**, *131*, 85−104.

(31) Char, B. W.; Geddes, K. O.; Gonnet, G. H.; Leong, B. L.; Monagan, M. B.; Watt, S. M. *Maple V language reference manual*; Springer-Verlag, Heidelberg 1992.

(32) Zaitsau, D. H.; Kabo, G. J.; Strechan, A. A.; Paulechka, Y. U.; Tschersich, A.; Verevkin, S. P.; Heintz, A. *J. Phys. Chem. A* **2006**, *110*, 7303−7306.

(33) The vibrational frequencies of the smallest species ((1, 0), (0, 1), (1, 1) and (2, 2)) are available as supporting information. The frequencies of all other clusters are available from the authors.

(34) This seemingly small cell contains, in fact, 64 [bmim][Tf] pairs, corresponding to 2112 atoms.

(35) Fredlake, C. P.; Crosthwaite, J. M.; Hert, D. G.; Aki, S. N. V. K.; Brennecke, J. F. *J. Chem. Eng. Data* **2004**, *49*, 954−964.

(36) Wahnström, G. *Phys. Rev. A: At., Mol., Opt. Phys.* **1991**, *44*, 3752−3764.

(37) See, for instance: Ku, B. K.; de la Mora, J. F. *J. Phys. Chem. B* **2004**, *108*, 14915−14923.

(38) Wang, Y.; Voth, G. A. *J. Am. Chem. Soc.* **2005**, *127*, 12192−12193.

(39) Canongia Lopes, J. N. A.; Padua, A. A. H. *J. Phys. Chem. B* **2006**, *110*, 3330−3335.

(40) Berg, R. W.; Deetlefs, M.; Seddon, K. R.; Shim, I.; Thompson, J. M. *J. Phys. Chem. B* **2005**, *109*, 19018−19025.

(41) Montanari, B.; Ballone, P.; Mazza, T.; Milani, P. *J. Phys. Cond. Matter* **2005**, *17*, 3787−3806.

(42) Kossmann, S.; Thar, J.; Kirchner, B.; Hunt, P. A.; Welton, T. *J. Chem. Phys.* **2006**, *124*, 174506.

(43) Youngs, T. G. A.; Del Pópolo, M. G.; Kohanoff, J. *J. Phys. Chem. B* **2006**, *110* 5697−5707.

(44) Levine, I. N. *Physical Chemistry*; McGraw Hill: New York, 2001.

(45) Valleau, J. P.; Torrie, G. In *Modern Theoretical Chemistry*; Berne, B., Ed.; Plenum Press: New York, 1977, Vol. 5.